Chapter 13
Centrifuge Model Tests at Zhejiang University for LEAP-ASIA-2019

Qiang Ma, Yan-Guo Zhou, Kai Liu, and Yun-Min Chen

Abstract Two centrifuge models with the same target relative density ($D_r = 65\%$) were conducted in different centrifugal acceleration (30 g for Model-A and 15 g for Model-B) at Zhejiang University (ZJU) to validate generalized scaling law in the program of LEAP-ASIA-2019. The same model used in LEAP-UCD-2017 was repeated, representing a 5-degree slope consisting of saturated Ottawa F-65 sand. This chapter describes test facilities, instrumentations layout, and test procedures. Uncertainty analysis is also carried out in input parameters (e.g., achieved peak ground acceleration, achieved density and the degree of saturation). The test results of acceleration, excess pore water pressures, and displacement etc. were compared at prototype scale to check the validity of the generalized scaling law (GSL). The preliminary experiment results of Zhejiang University show that the Type II generalized scaling law is applicable to the acceleration response while has a weak applicability to the displacement response.

Keywords Liquefaction Experiments and Analysis Projects (LEAP-ASIA-2019) · Generalized Scaling Law (GSL) · Centrifuge modelling

13.1 Introduction

LEAP (Liquefaction Experiments and Analysis Projects) is an international effort, which aims to provide a set of high quality laboratory and centrifuge test data to assess the capabilities of the advanced constitutive and numerical models developed in recent years for liquefaction problems (e.g., Kutter et al., 2014; Manzari et al., 2014). The results of LEAP-KU-2013 and 2014 showed some inconsistency between different centrifuge tests due to the differences of laminar containers,

Q. Ma · Y.-G. Zhou (✉) · K. Liu · Y.-M. Chen
MOE Key Laboratory of Soft Soil and Geoenvironmental Engineering, Institute of Geotechnical Engineering, Center for Hypergravity Experiment and Interdisciplinary Research, Zhejiang University, Zhejiang, Hangzhou, P. R. China
e-mail: qzking@zju.edu.cn

which caused challenges for numerical simulations (Tobita et al., 2014). Therefore, rigid boxes were adopted since in LEAP-GWU-2015 to avoid the numerical modeling complexities associated with the special boundary conditions created by different types of laminar containers. In the summary of LEAP-GWU-2015, Kutter et al. (2018) suggested that more rigorous site investigation should be used to determine the density and saturation of the soils (such as in-fight CPT testing, bender elements testing etc.). New methods such as high-speed cameras with PIV analysis are also recommended to trace dynamic surface lateral displacement. Thus, better practical experimental technology and measuring techniques were adopted in LEAP-UCD-2017, including in-flight CPT testing for estimating soil density, high-speed camera for tracing marker displacement as well as in-flight shear-wave velocity for detecting initial state of the model (Zhou et al., 2018).

LEAP-ASIA-2019 was organized based on two objectives: one is to validate the Type II generalized scaling law, the other one is to fill the gaps and further update the CPT tip resistance-density correlation obtained in the LEAP-UCD-2017 (Carey et al., 2018a, b). Ten centrifuge teams have performed at least two types of tests, the first one is conducted considering the traditional centrifuge scaling law and the second one is the same geometry as the first one but executed considering the generalized scaling law.

In LEAP-ASIA-2019, two centrifuge models were conducted at Zhejiang University to check the validity of the generalized scaling law. Large geotechnical centrifuge ZJU-400, uniaxial hydraulic shaker, and advanced in-flight bender element (BE) system, other unique techniques, including a two-dimensional in-flight miniature CPT system, bending disk system (BD) and high-speed cameras were also used in this study. Zhejiang University rigorously followed the specifications and procedures and gained reliable results. The achieved density of two models is close to the target density of $D_r = 65\%$, and the achieved degree of saturation $S_r > 99.5\%$. The input motion was well controlled and matched the target values. This chapter first describes test facilities, model preparations, and test procedures. Then uncertainty analysis is carried out in input parameters, such as achieved peak ground acceleration (PGA) and achieved density. Some preliminary experimental results are discussed in prototype scale as well, which contribute to further researchers to understand the experimental benchmark data of Zhejiang University in LEAP-ASIA-2019.

13.2 Test Facilities and Specifications

13.2.1 Test Facilities

LEAP-ASIA-2019 tests of Zhejiang University were performed by using the ZJU-400 centrifuge with in-flight uniaxial shaker and bender elements /bending disks testing system, which was detailed introduced in Zhou et al. (2018), Liu et al. (2020).

The same rigid model container was used as LEAP-UCD-2017, which had the inner dimension of 770 mm long, 400 mm wide, and 500 mm deep. The container was then shortened to 666 mm in length to match the prototype specification of 20 m in length. The supporting blocks are 52 mm thick aluminum plate, which was braced at six locations and bolted to the end walls of the container, demonstrated in Fig. 13.1. The blocks were well sealed to prevent drainage along the aluminum container interfaces.

A two-dimensional miniature CPT system used in LEAP-UCD-2017 was applied to evaluate the uniformity and density of the soil models before and after each destructive motion. The size of cone tip was 6 mm in diameter with apex angle of 60°.

13.2.2   Model Geometry and Instrumentations Layout

Two models conducted in LEAP-ASIA-2019 had the same geometry as LEAP-UCD-2017, representing a 5-degree, 4 m deep at midpoint, 20 m long sand slope deposit of Ottawa F-65 sand at prototype scale. The soil surface normal to slope direction was not curved according to the radius of the centrifuge because the shaking direction is parallel to the axis of the centrifuge, and the centrifuge radius (4.5 m) is larger enough to mitigate the effect of ground curve.

Figure 13.1 illustrated the instrumentations locations in the model. Four horizontal accelerometers (AH1-AH4) and four pore pressure transducers were located at the midpoint along the shaking direction to minimize the boundary effects from the rigid walls. Two additional accelerometers (AH11 and AH12) were attached on the bottom of container to record the achieved base motion. Two vertical accelerometers were installed at the top of the container to monitor vertical and rocking accelerations. Another four horizontal accelerometers and two pore pressure transducers (AH6, AH7, AH9 and AH10; P6, P8-P10) were included at equivalent depths as sensors in the central array and were intended to help in understanding the effect of the container boundaries on the model response. Three pairs of bender elements, at the depth of 1 m, 2 m, and 3 m respectively, were placed to measure vertically polarized and horizontal travelling SV shear-wave velocity. A pare of bending disks were also installed to measure P-wave velocity after model saturation.

Eighteen (3 rows × 6 columns) specified surface markers were placed at the surface of the soil to trace the deformation during soil liquefaction. The specified surface markers were red shown in Fig. 13.2, which made by a 10 mm length, 25 mm in diameter PVC tube with an aluminum cross bar fixed in center. The black surface markers made of zip ties were also employed and all the surface markers were installed in a 50 mm × 50 mm grid (model scale). Twelve colored (blue) sand columns were used to curve lateral spreading profile by excavation after the final spin down.

Five high-speed cameras (GoPro cameras) were installed on the camera frame to record the lateral displacement of surface markers on different regions of the model during spinning. The model is photographed in Fig. 13.2.
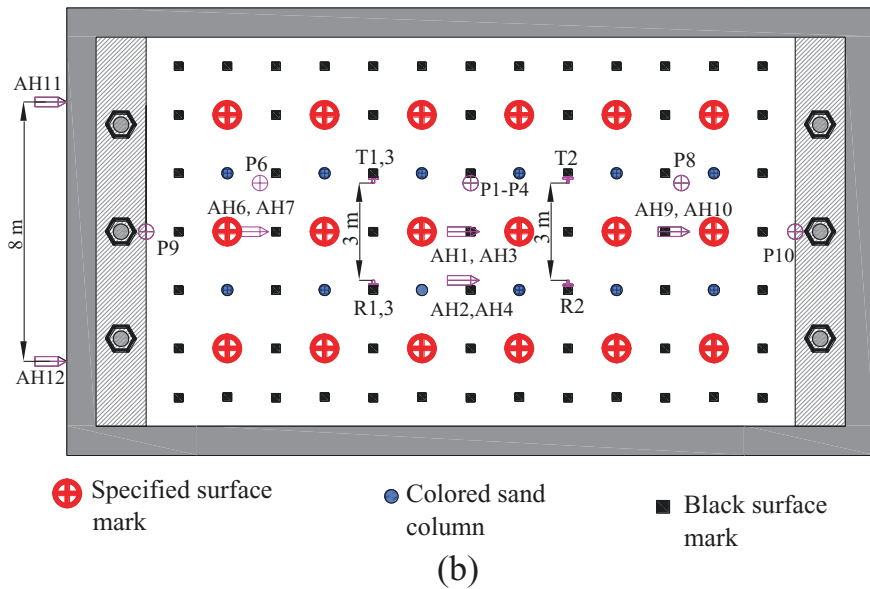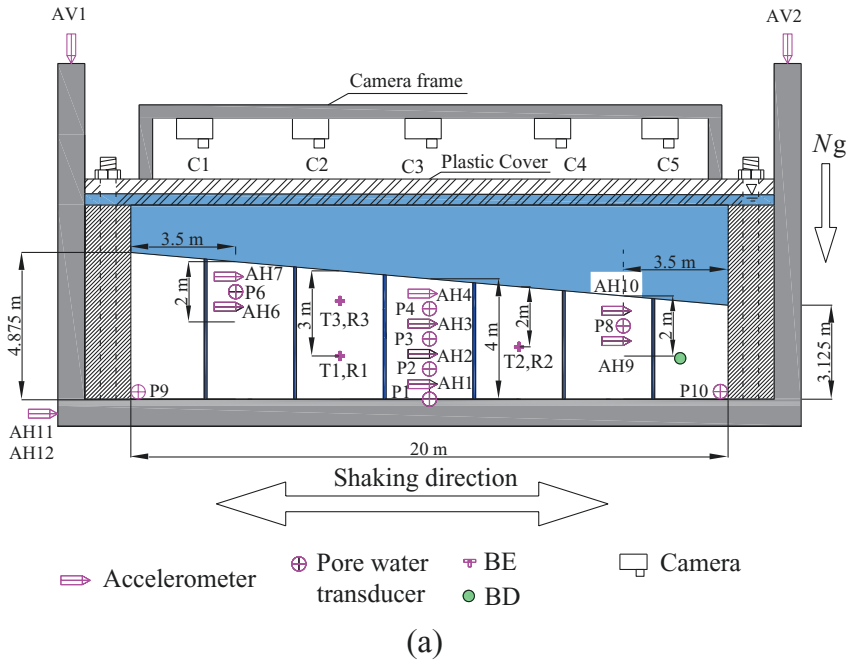
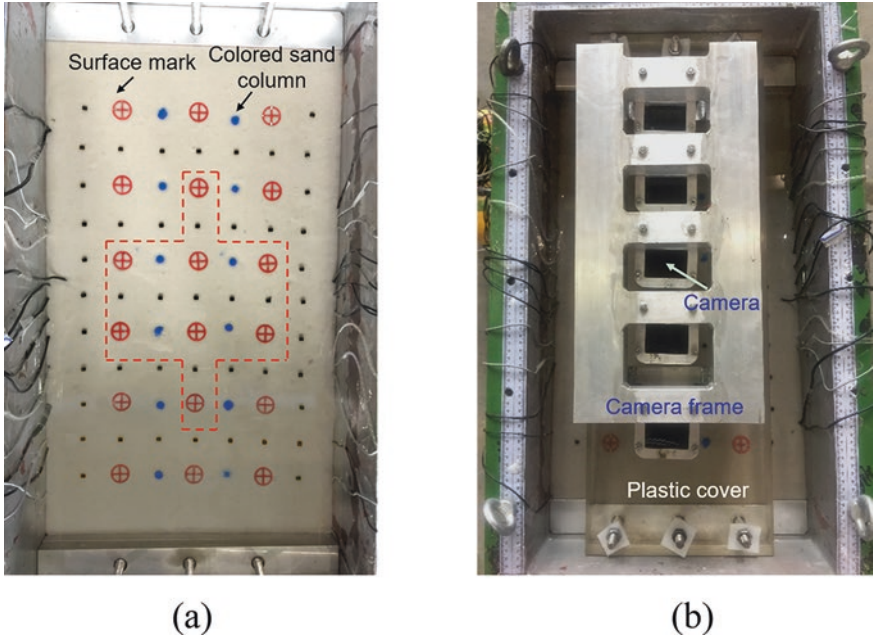**Fig. 13.1** Model geometry and instrumentations layout (prototype scale): (**a**) side view; (**b**) top view

Fig. 13.2 Photograph of finished model: (**a**) surface markers and colored sand columns; (**b**) high-speed cameras

13.3 Model Preparation

13.3.1 Test Material

The same Ottawa F-65 sand was used as the LEAP-UCD-2017, the grain size distribution curve, physical properties and additional material properties of Ottawa F-65 sand, including triaxial, simple shear, and permeability test data, could be found in Carey et al. (2017).

13.3.2 Scaling Law

One of the objectives of LEAP-ASIA-2019 is the verification of the generalized scaling law. The Type II generalized scaling law (GSL) was applied in the experiment consequently, which contains two stages. In the stage I of generalized scaling law, the prototype is scaled down into a virtual model using a 1 g filed scaling law proposed by Iai (1989) with a scaling factor μ. In the stage II of generalized scaling law, the virtual model is scaled down into the physical model applying the conventional centrifuge scaling law with a scaling factor η. By this means, the overall

Table 13.1 Generalized scaling factors implemented in ZJU experiment

| | Scaling factors (prototype/model) | | |
	GSL	Model-A	Model-B
1 g	μ	1	2
Centrifuge	η	30	15
Length	$\mu\,\eta$	30	30
Time	$\mu^{0.75}\,\eta$	30	25.2
Density	1	1	1
Frequency	$\mu^{-0.75}\,\eta^{-1}$	1/30	1/25.2
Acceleration	$1/\eta$	1/30	1/15
Displacement	$\mu^{1.5}\,\eta$	30	42.4
Stress	μ	1	2
Strain	$\mu^{0.5}$	1	1.4
Permeability	$\mu^{0.75}\,\eta$	30	25.2
Pore pressure	μ	1	2

geometric scaling factor of GSL is $\lambda = \mu\eta$, which is much larger than that of conventional centrifuge scaling law ($\lambda = \eta$). More detailed description of GSL could reference Iai et al. (2005).

In the program of LEAP-ASIA-2019, two models were designed with the same overall scaling factor ($\lambda = 30$) using the Iai's Type II scaling law, called Model-A (30 g), Model-B (15 g) respectively. Model-A was regarded as a virtual prototype and Models-B was supposed to model the prototype. The generalized scaling factors used in this study were listed in Table 13.1.

13.3.3   Model Preparation and Saturation

Air pluviation method was adopted to ensure a high level of uniformity when preparing the models. The calibration was implemented before pluviating the model. The target density is $\rho_d = 1654$ kg/m³. The achieved densities were calculated by the measurements of soil mass and volume and the best estimated final achieved density was detailed in Table 13.2. Though the achieved density was slight loose than the target, the density of two models was nearly identical.

The viscous fluid used to saturation was silicone oil with density of 0.95 g/cm³ (25 °C). The target viscosity is 30 times of viscosity of water (30 cSt) for Model-A, 25.2 cSt for Model-B according to the generalized scaling law listed in Table 13.1, which aims to overcome the conflict between dynamic and consolidation time scaling factors (Dewoolkar et al., 1999). Temperature-fluid viscosity calibration curves were obtained before saturation by using a MCR302 rotational rheometer (manufacturer: Anton Paar), which was shown in Fig. 13.3. The viscosity decreases with an increase of temperature. Owing to the spin of centrifuge, the temperature of

Table 13.2 Achieved density for each model

Model	Mass of sand	Volume after saturation	Average density ρ_d
	g	cm³	kg/m³
Model-A	59,098	36,376.8	1625 ± 11
Model-B	60,103	36,812.4	1633 ± 11
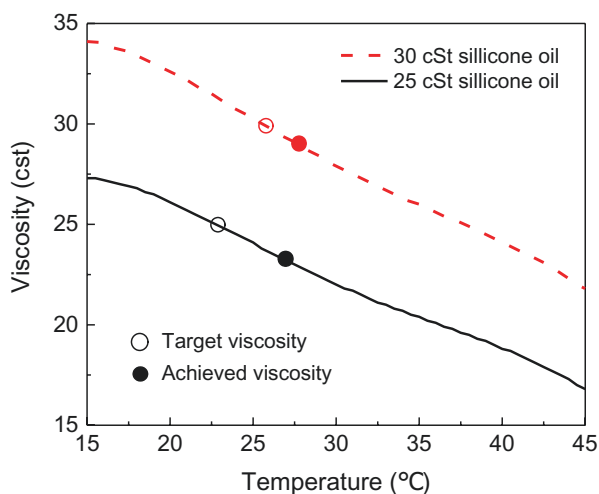
Fig. 13.3 Temperature-fluid viscosity curve of silicone oil

silicone oil commonly increases by 2–3 °C, which has a very limited influence on the viscosity of silicone oil.

When saturation, the oil tank and model container were kept under the same vacuum level (around −95 kPa) and the oil was firstly de-aired more than 24 h. Then transport silicone oil from the reservoir to the container was driven by gravity feed. The saturation speed was controlled to prevent soil disturbance at the bottom of container. When saturation was accomplished, bending disk testing system was used to check the degree of saturation. Figure 13.4 represents the typical BD test result, the measured V_p around 1160 m/s. According to Zhou et al. (2018), the achieved the degree of saturation Sr is higher than 99.5%.

13.3.4   Input Motion

The input base acceleration for each model consisted a sequence of three destructive motions with the same maximum acceleration of 0.25 g (prototype scale). All the motions represented 1 Hz ramped sine wave with 16 cycles, shown in Fig. 13.5.
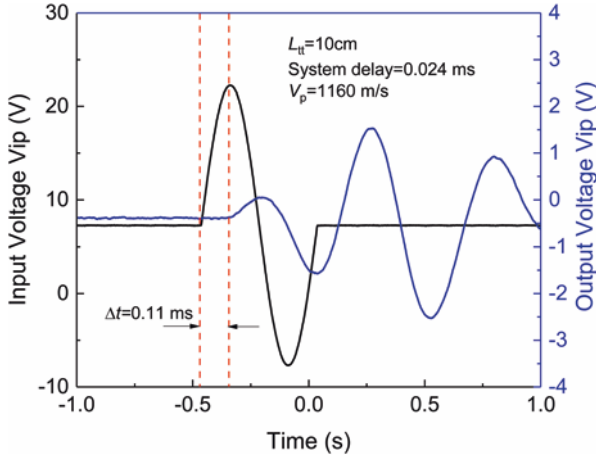
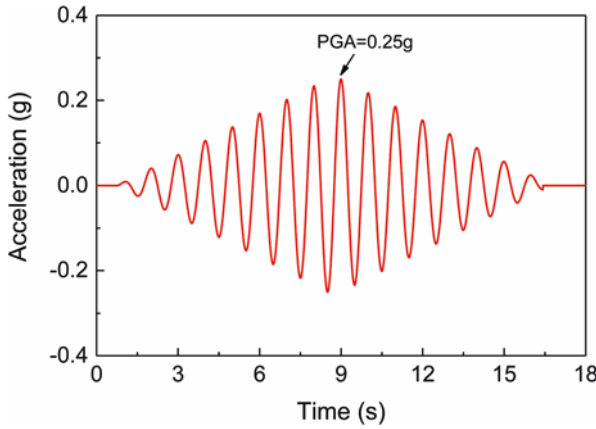**Fig. 13.4** Typical signal of BD test

Fig. 13.5 Acceleration time history for the destructive motion

13.4   Test Procedures and Achieved Motions

13.4.1   Test Procedures

The test procedures were shown in Fig. 13.6. Before the centrifuge spin up, a careful survey of the surface markers was carried out and the temperature of silicone oil was measured. Then the centrifuge was spun up to 10 g, 20 g, and 30 g step by step (7.5 g and 15 g for Model-B). When the pore pressure was stable at each g-level, the shear wave velocity was measured by using BE testing system. After reaching the target centrifugal acceleration, the model then was subjected to a non-destructive step wave, which is used to characterize the model. The CPT test was carried out to
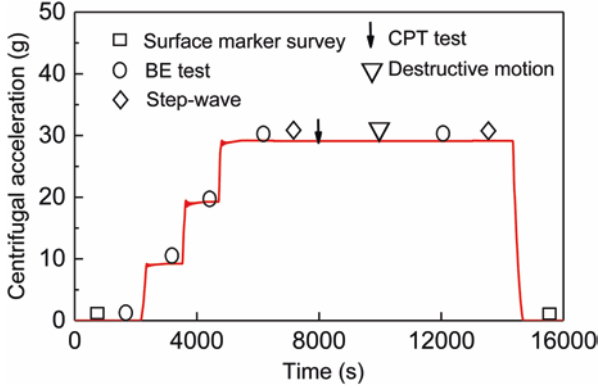
Fig. 13.6 Test procedures and shaking sequences

determine the density of the model before each destructive motion. After that, a destructive motion (shown in Fig. 13.5) was executed and then, another step-wave conducted when the excess pore pressure was fully dissipated. The centrifuge was spun down step by step and V_s was measured at each step after all the above procedures accomplished. Finally, surface markers and temperature were measured. Each model and each motion followed the same procedure except Model-B second motion missing the step-wave after destructive motion. Each model contains three cycles of abovementioned procedures.

13.4.2   In-Flight Measurement

CPT tests were conducted in 30 *g* for Model-A and 15 *g* for Model-B with the velocity of penetration 0.6 mm per second and sample rate 1 Hz. One of the key parameters controlling tip resistance is effective stress (Jamiolkowski et al., 1985), so dimensional analysis was adopted to eliminate the influence of stress caused by different centrifugal acceleration. Figure 13.7 demonstrated the normalized tip resistance (defined in Eq. (13.1)) versus normalized depth (defined in Eq. (13.2)) for two models.

$$Q = \frac{q_c}{\sqrt{\sigma_v' p_a}}$$

(13.1)

$$Z = \frac{z}{B}$$

(13.2)

where q_c and σ_v' is tip resistance and vertical effective stress, expressed in MPa, p_a is atmospheric pressure, 101 kPa; z is penetration depth, B is cone diameter, 6 mm.
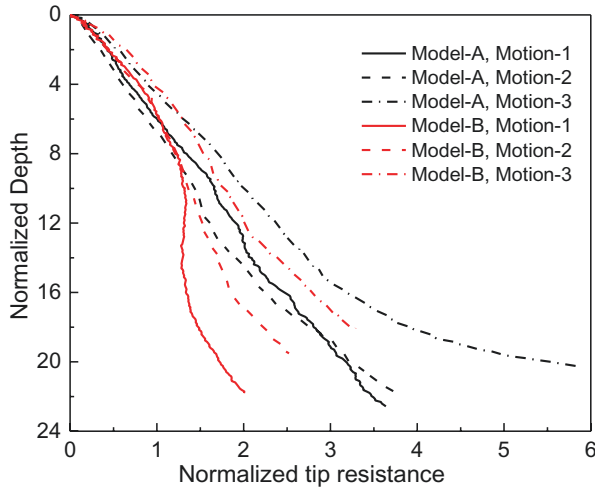
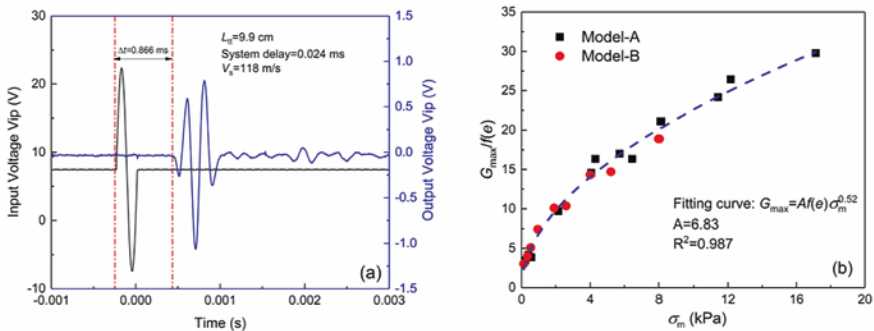**Fig. 13.7** Normalized cone tip resistance

Fig. 13.8 The results of bender disks: (**a**) typical signal of BE tests; (**b**) fitted Hardin curve of Ottawa-F65 sand

The normalized resistance was nearly linearly increased, which indicated the uniformity of both two models. According to Kim et al. (2016), the slope of the curve represents the relative density of sand. The result indicated that Model-A and Model-B have a comparable density, which agreed with Table 13.2 results.

Three pairs of bender elements were used to measure the V_s of model. Figure 13.8a gives a typical signal of BE during spinning, indicating the arrival of receiver is well distinguishable to ensure the reliability of BE results. Figure 13.8b shows the fitted Hardin curve of Ottawa-F65 sand, G_{max} was calculated through Eq. (13.3):

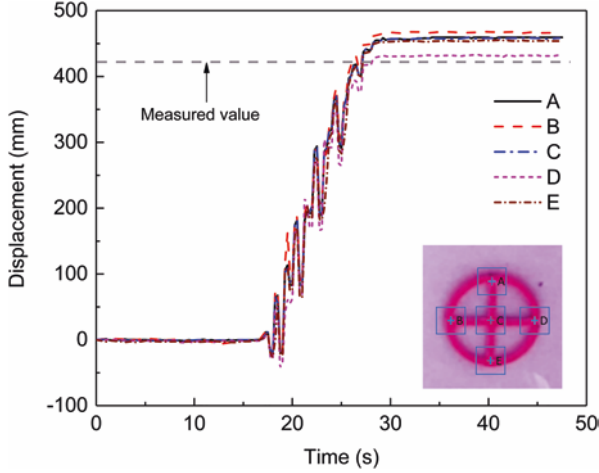$$G_{max} = \rho V_s^2$$

$$(13.3)$$

Fig. 13.9 Time history of lateral displacement obtained by PIV analysis

in which V_s is the shear wave velocity measured by BE testing in different stable g-level.

As shown in Fig. 13.1a, five high-speed GoPro cameras were installed above the slope surface to record movement of surface markers during the destructive motion. The videos were converted to displacement time history by Geo-PIV analysis procedure (e.g., White et al., 2003). Five points located at different region of the surface marker were analyzed to ensure reliable results. Figure 13.9 demonstrates typical results of dynamic displacement of one surface marker from five points, showing high consistency within five points. The residual displacement value obtained using videos agreed with that measured by hand afterwards.

13.4.3 Achieved Motions

In dynamic centrifuge testing, it is crucial to impose acceleration to models which is as close as possible to the target acceleration. Assessment of the similarities and differences between achieved input and target motions is fundamental to address the LEAP validation objectives. The concept of effective PGA was adopted to evaluate the accuracy and efficiency of the motions. The effective PGA, PGA_{eff}, is defined as below:

$$PGA_{eff} = PGA_{1Hz} + 0.5 \times PGA_{hf} \tag{13.3}$$

in which PGA_{hf} represents the peak acceleration of the high frequency component of the motion, PGA_{1Hz} denotes the peak acceleration which was isolated by use of a notched band pass filter with corner frequencies of 0.5 and 1.2 Hz. The results of all

Table 13.3 The effective PGA of Motion-1 (unit: g)

Model	Accelerometer	PGA_{tar}	PGA_{1Hz}	PGA_{hf}	PGA_{ach}	PGA_{eff}
Model-A	A11	0.25	0.184	0.171	0.354	0.270
	A12		0.195	0.18	0.374	0.285
Model-B	A11	0.25	0.205	0.147	0.347	0.279
	A12		0.204	0.146	0.345	0.277
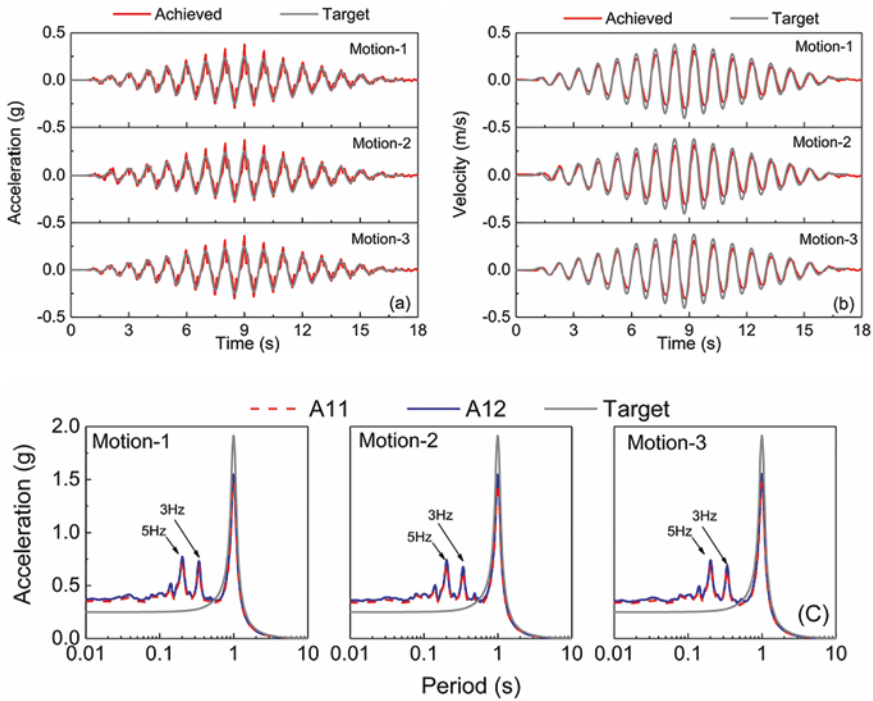
Fig. 13.10 Comparison between target and achieved motions of Model-A: (**a**) acceleration time history; (**b**) velocity time history; (**c**) acceleration response spectra

the input motions for two models are summarized in Table 13.3. It is found that PGA_{1Hz} values of AH11 are smaller than AH12 for Model-A, while almost the same between AH11 and AH12 for Model-B, indicating that there was a small angle between AH11 and motion direction in Model-A.

Figure 13.10a, b compare the achieved and target acceleration time histories and velocity histories for Model-A three motions, the velocity time series obtained by integrating acceleration. The achieved PGA usually 10–20% higher than target PGA, while the achieved PGV only about 90% of target one, which is because the achieved motion contained high frequency components. Five percent damped acceleration response spectra (ARS) for model-A three motions are shown in Fig. 13.9c, the average achieved peak spectral acceleration at T = 1 s is 1.5 g, lower than target

one (approximately 1.9 *g*). Figure 13.10c also indicates that the achieved motion contained some higher frequency components especially in 3 Hz and 5 Hz.

Figure 13.11 gives information about the measured vertical motions for Model-A, Motion-2. The grey lines indicate the unfiltered motions and the black lines are band-pass (0.3–3 Hz) filtered motions. Although zero vertical acceleration is expected during shaking, the hydraulic shaker produced unintended vertical component in addition to the desired horizontal accelerations. Besides, Coriolis acceleration will also contribute to the measured vertical acceleration. Little phase shift between AV1 and AV2 is observed from Fig. 13.11, revealing that the container was a negligible rocking during shaking.

13.5 Test Results

13.5.1 Acceleration Responses

Figure 13.12a shows acceleration time histories of Motion-1 in Model-A, other results in ZJU experiments are similar with the instance. The acceleration time histories show de-amplification in upslope direction and significant negative dilation spikes in downslope direction for AH1-AH4, which have been observed in LEAP-GWU-2015 and LEAP-UCD-2017 (e.g., Carey et al., 2018a, b). The spikes tend to be most exaggerated near the slope surface where the soil easily dilated. When the sharp spikes occurred, the waveform significantly changes both in frequency and
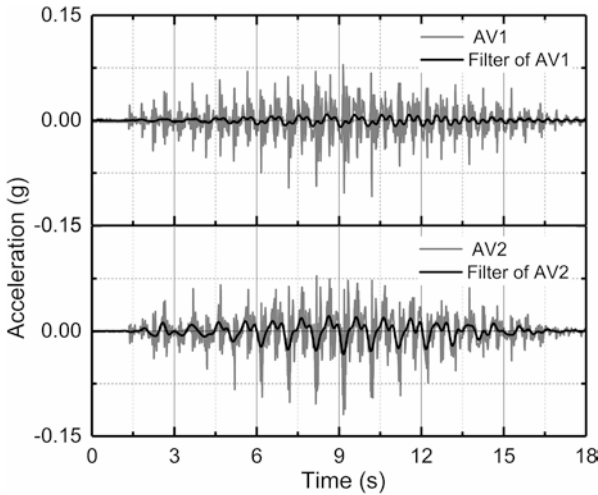

Fig. 13.11 Vertical accelerations on container ends of Model-A during Motion-2
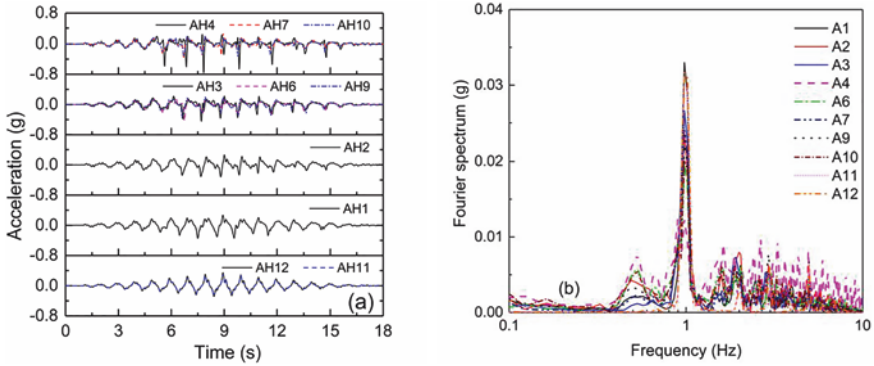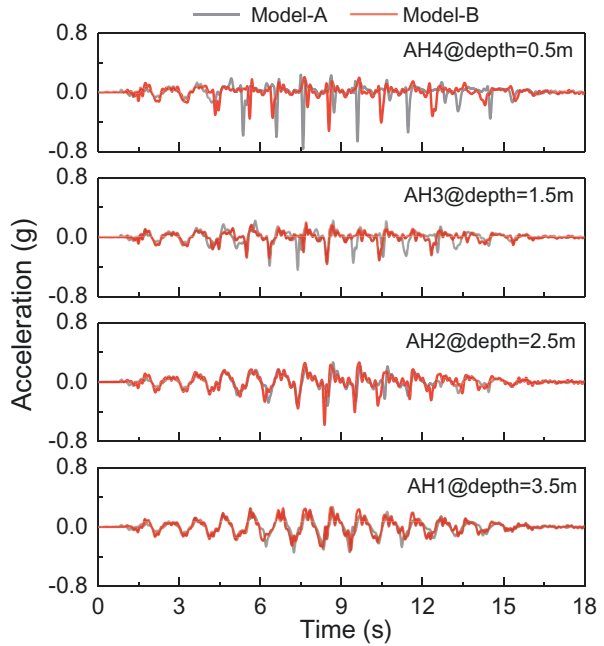
Fig. 13.12 Acceleration response of Model-A, Motion-1: (**a**) time histories; (**b**) fourier spectrums

Fig. 13.13 Acceleration
response between Model-A
and B, Motion-1

amplitude from the base motion. Figure 13.12b demonstrates the Fourier spectrums, some higher frequency occurred owing to dilation of soil.

Figure 13.13 contrasts the central array acceleration response of two models during Motion-1. The time histories of acceleration for two models show a high consistency not only in trends but also in value, which reveals that GSL is applicable to acceleration response in the experiments.

13.5.2 Pore Pressure Response

Figure 13.14 compares the central vertical array of time histories of excess pore pressure ratio r_u ($\Delta u/\sigma_v'$) for Motion-1 in Model-A and Model-B. P1, P2, P3, and P4 were specified to be at depths of 1, 2, 3, and 4 m respectively, and the initial vertical effective stresses are approximately 10, 20, 30, and 40 kPa respectively. The process of excess pore-water pressure build-up during shaking shows a significant agreement. Severe liquefaction occurred in all three models throughout the soil layer and significant dilatancy spikes are observed over the whole depth of the slope, implying that the motion is strong enough to liquefied the slope from top to the bottom. The time required for excess pore-water dissipation, however, shows a discrepancy. Model-B need a longer duration time for pore-water dissipation in prototype scale than the others with higher centrifugal accelerations. A significant discrepancy in dissipation time also has been reported by Tobita et al. (2011) when Type II GSL is applied into saturated flat ground. They assumed that three possibilities may contribute to this phenomenon: (a) effect of duration time for consolidation before shaking; (b) effect of low effective confining stress on the scaling law; (c) possible change of permeability of the model ground due to absorption of the pore fluid on sand particles.

Fig. 13.14 Pore pressure time history: Motion-1
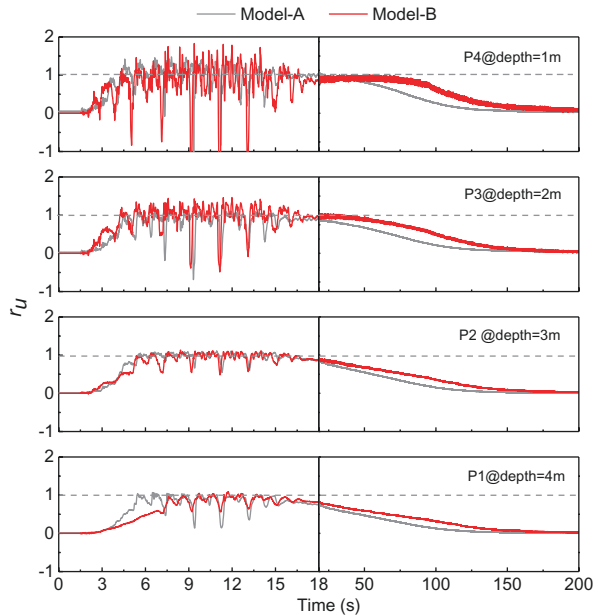
13.5.3   Displacement Response

For all experiments, similar trends are observed that the soil surface settles at the top of the slope higher than toe. A typical result (Model-A) shown in Fig. 13.15. Significant settlement at the top of the slop was occurred during the first motion while heave was observed in the toe. Then the settlement decreased with the number of motions dramatically for the destructive motions densified the soil. Noticing that Motion-3 nearly had a uniform settlements along the slope, no apparent heave at toe of the slope.

Table 13.4 lists the average horizontal displacement D_h and standard deviation of vertical displacement σ for each motion, which calculated from only red surface marker which located in red dotted line frame shown in Fig. 13.2a. Compared the average horizontal displacement of Model-A and B for each motion, some discrepancies were observed. The horizontal displacement of Model-A larger than Model-B during the Motion-2 and 3, whereas significantly smaller in Motion-1. Based on the results of two tests, GSL has a weak applicability to displacement response. Standard deviation of Model-B larger than Model-A indicating more scatter for the vertical displacement of Model-B. The scaling factor of displacement in the GSL is much larger for Model-B than A, any little measurement error would be amplified significantly and scattered the data. Hence, special care had to be taken in measurement of ground displacement when applied the GSL.

The lateral displacement profiles in Fig. 13.15 were obtained from excavation of colored sand columns. The profiles show that the displacement distributed over the whole depth and reached maximum at the surface. Consistent with the observation of surface spreading, the lateral displacements near the side walls were also smaller than those at the mid-slope.
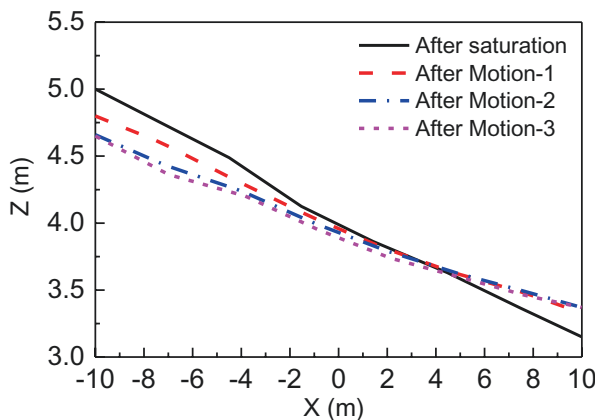

Fig. 13.15 The development of surface settlements (Model-A)

Table 13.4 Average values of lateral displacement after each motion (unit: mm)

	Motion-1		Motion-2		Motion-3	
Model	D_h	σ	D_h	σ	D_h	σ
A	393.75	30.70	187.50	30.00	110.63	37.45
B	593.97	114.73	137.89	47.43	45.08	16.56

13.6 Summary and Conclusions

Two centrifuge tests were conducted at Zhejiang University in LEAP-ASIA-2019 which were designed in the same target densities and subjected three motions under centrifugal acceleration of 30 g and 15 g respectively. Generalized scaling law was applied in the tests to verify the application of the Type II GSL. In this chapter, information on test facilities, model setup and preparation, test procedures, in-flight characterizations, and analysis of the achieved motion and preliminary tests results was presented.

The facilities adopted in LEAP-ASIA-2019 were the same as LEAP-UCD-2017. Besides the bending disk system was carried out to evaluate the degree of saturation. MCR302 rotational rheometer was used to gain temperature-fluid viscosity curve of silicone oil. The achieved viscosity of both two models was close to the target viscosity.

The achieved densities in both models were a bit loose than target one. The CPT results indicated that two models had a closed density. The achieved PGA usually 10–20% higher than target PGA, while the achieved PGV only about 90% of target one. The achieved effective PGA, PGA_{eff}, for each motion roughly matches the targets. Five percent damped ARS shows the achieved motions were smaller than the target of 1 Hz components and some high frequency components were observed in input motion. The vertical accelerations at opposite ends of container were small, indicating a negligible rocking effect during shaking.

Typical results were exampled to explain the response of two models. Liquefaction was occurred in the whole slope. Both of two models had similar acceleration response and pore water response. Spikes due to dilatancy were observed in acceleration time history, which are consistent with drops in excess pore pressure. The dissipation time of pore-water pressure shown a discrepancy two models. Lateral and vertical displacements for each motion were surveyed via some surface markers. The tests result of displacements shown a similar trend but different in value, indicating a weak applicability to the displacement response.

The above results show a promising applicability of GSL especially in modelling larger-scale prototype. However, the scaling factor of displacement in the Type II GSL is much larger than conventional scaling law if a large μ was adopted. Any little measurement error would be amplified significantly. So, special care had to be taken in measurement of ground displacement when usage of Type II GSL.

References

Carey, T. J., Kutter, B. L., Manzari, M. T., & Zeghal, M. (2017). *LEAP soil properties and element test data*. https://datacenterhub.org/resources/leap_soil.

Carey, T., Gavras, A., Kutter, B., Haigh, S. K., Madabhushi, S. P. G., Okamura, M., Kim, D. S., Ueda, K., Hung, W. Y., Zhou, Y. G., Liu, K., Chen, Y. M., Zeghal, M., Abdoun, T., Escoffier, S., & Manzari, M. (2018a). *A new shared miniature cone penetrometer for centrifuge testing*. In 9th international conference on physical modelling in geotechnics, ICPMG 2018 (pp. 293–298). CRC Press/Balkema.

Carey, T. J., Hashimoto, T., Cimini, D., & Kutter, B. L. (2018b). LEAP-GWU-2015 centrifuge test at UC Davis. *Soil Dynamics and Earthquake Engineering, 113*, 663–670.

Dewoolkar, M. M., Ko, H. Y., Stadler, A. T., & Astaneh, S. M. F. (1999). A substitute pore fluid for seismic centrifuge modeling. *Geotechnical Testing Journal, 22*(3).

Iai, S. (1989). Similitude for shaking table tests on soil-structure-fluid model in 1 *g* gravitational field. *Soils and Foundations, 29*(1), 105–118.

Iai, S., Tobita, T., & Nakahara, T. (2005). Generalised scaling relations for dynamic centrifuge tests. *Geotechnique, 55*(5), 355–362.

Jamiolkowski, M., Ladd, C. C., Germaine, J. T., & Lancellotta, R. (1985). *New development in field and laboratory testing of soils*. In Proceedings of the 11th ICSMFE (Vol. 1, pp. 57–153).

Kim, J. H., Choo, Y. W., Kim, D. J., & Kim, D. S. (2016). Miniature cone tip resistance on sand in a centrifuge. *Journal of Geotechnical and Geoenvironmental Engineering, 142*(3), 04015090.

Kutter, B. L., Manzari, M. T., Zeghal, M., Zhou, Y. G., & Armstrong, R. J. (2014). Proposed outline for LEAP verification and validation processes. In *Geotechnics for catastrophic flooding events* (pp. 99–108). CRC Press.

Kutter, B. L., Carey, T. J., Hashimoto, T., Zeghal, M., Abdoun, T., Kokkali, P., et al. (2018). LEAP-GWU-2015 experiment specifications, results, and comparisons. *Soil Dynamics and Earthquake Engineering, 113*, 616–628.

Liu, K., Zhou, Y. G., She, Y., Meng, D., Xia, P., Huang, J. S., et al. (2020). Specifications and results of centrifuge model test at Zhejiang University for LEAP-UCD-2017. In *Model tests and numerical simulations of liquefaction and lateral spreading: LEAP-UCD-2017* (pp. 401–419). Springer.

Manzari, M. T., Kutter, B. L., Zeghal, M., Iai, S., Tobita, T., Madabhushi, S. P. G., et al. (2014). LEAP projects: Concept and challenges. In *Geotechnics for catastrophic flooding events* (pp. 109–116). CRC Press.

Tobita, T., Iai, S., Tann, L. V., & Yaoi, Y. (2011). Application of the generalized scaling law to saturated ground. *International Journal of Physical Modelling in Geotechnics, 11*(4), 138–155.

Tobita, T., Manzari, M. T., Ozutsumi, O., Ueda, K., Uzuoka, R., & Iai, S. (2014). *Benchmark centrifuge tests and analyses of liquefaction-induced lateral spreading during earthquake*. Taylor and Francis.

White, D. J., Take, W. A., & Bolton, M. D. (2003). Soil deformation measurement using particle image velocimetry (PIV) and photogrammetry. *Geotechnique, 53*(7), 619–631.

Zhou, Y. G., Sun, Z. B., & Chen, Y. M. (2018). Zhejiang University benchmark centrifuge test for LEAP-GWU-2015 and liquefaction responses of a sloping ground. *Soil Dynamics and Earthquake Engineering, 113*, 698–713.